



Cite this: *Soft Matter*, 2019,
15, 2999

Received 23rd January 2019,
Accepted 27th February 2019

DOI: 10.1039/c9sm00159j

rsc.li/soft-matter-journal

Collective oscillation in dense suspension of self-propelled chiral rods†

Yan Liu,^a Yuguang Yang,^b Bo Li  *^a and Xi-Qiao Feng  ^a

Active particles capable of self-propulsion commonly exhibit rich collective dynamics and have attracted increasing attention due to their applications in biology, robotics, social transport, and biomedicine. However, it remains unclear how the geometric features of active particles affect their collective behaviors. In this paper, we explore the collective dynamics of L-shaped active rods. We show that a dense suspension of self-propelled L-shaped rods exhibits fascinating non-equilibrium oscillatory dynamic clustering. A new oscillation phase can form due to distinct collisions and aggregation mechanisms arising from the L-shaped chirality of elements. A generic diagram of emerging states is provided over a wide range of geometric parameters. Our findings show that the comparative strength between the periodic separation and proximity effect from chirality and the alignment effect from elongated geometry drive the formation and transition of dynamic patterns. This chirality-triggered oscillation phase suggests a new route to understand active matter and paves a way for emerging applications.

1. Introduction

Systems consisting of multiple active particles have attracted mounting interest, ranging from biological entities to synthetic microswimmers.^{1–8} Compared to independent individual movements, collective motions of active particles bear many fascinating advantages. For example, a bacterial colony can more easily populate new territories, search for food, and increase its survival probability under harsh conditions. Swarming is also an effective strategy to prevail against antibiotics.^{9–11} Moreover, microscopic particles energized by external fields enable many fascinating applications, such as fabricating complex structures *via* self-assembly, sorting, and alignment.^{12–16}

Active particles, which are self-propelled by utilizing energy from their environment, exhibit a wealth of novel collective behaviors that are not attainable in passive particles at thermal equilibrium. For example, large-scale collective dynamics has been systematically observed in active particle systems including swirling,^{17,18} rotation,¹⁹ and giant number fluctuation.²⁰ With geometric anisotropy, active rod-shaped particles can exhibit some distinct dynamic features compared to spherical particles. It has been reported that active rods such as *Bacillus subtilis* can spontaneously exhibit nematic and laning phases, depending on

the aspect ratio of the rods.²¹ This reveals that the shape of active particles plays a significant role in collective motions.

So far, most studies on collective motions of active particles have focused on objects bearing a symmetric form such as spherical and rod-like shapes.^{22–24} However, active motions of particles with an asymmetric shape beg thorough investigation. On the one hand, asymmetric forms of active particles have been widely observed in living systems. For example, vibrioid or helical morphologies are common among bacteria,²⁵ such as *Caulobacter crescentus* of a crescent shape and *Helicobacter pylori* of a helix form.^{26–28} Studying the specific migration modes of bacteria with unusual geometries is crucial for understanding their surviving and colonizing. On the other hand, the asymmetric shape can endow the microswimmer with a torque and result in chiral active Brownian motion, *i.e.* circular motion (in two dimensions) and helicoidal motion (in three dimensions) with well-defined chirality.^{13,29–33} This chirality may provide novel bottom-up strategies for engineering artificial structures with unique physical properties.^{34–38}

In this work, we investigate the two-dimensional (2D) collective dynamics of self-propelled rods with L-shaped chirality (Fig. 1a). We show that chiral L-shaped rods exhibit collective dynamics which differs markedly from that of straight rods.^{22,39,40} Through large-scale simulations, we discover a novel collective oscillation phenomenon, which is attributed to the circular motion arising from chirality. A phase diagram is established to identify how the length ratio and angle of two arms of the L-shaped rods dictate the collective dynamics of the system. Various evidences are provided to explain the formation of oscillatory phases and the distinct collective dynamics observed in chiral rod systems.

^a Institute of Biomechanics and Medical Engineering, AML,
Department of Engineering Mechanics, Tsinghua University, Beijing 100084,
China. E-mail: libome@tsinghua.edu.cn

^b Chemical & Biomolecular Engineering, Johns Hopkins University, Baltimore,
MD 21218, USA

† Electronic supplementary information (ESI) available. See DOI: 10.1039/c9sm00159j

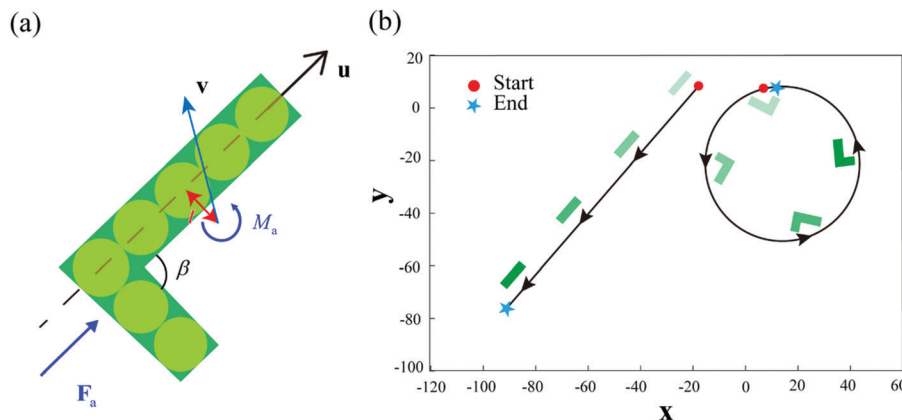


Fig. 1 (a) A chiral L-shaped rod model with an active force \mathbf{F}_a and a torque M_a . The eccentricity of the rod is denoted by l , representing the effective distance between the center of mass and the midline of the long axis. The orientation of the rod is denoted by \mathbf{u} . The translational velocity \mathbf{v} is different from its orientation direction. (b) Trajectories of a chiral and an achiral rod with self-propulsion. An isolated chiral rod performs circular motion with a period given by eqn (3), while an achiral rod performs linear motion. Darkness of the color shade represents time.

Finally, we make general discussions and report our conclusions. Our findings demonstrate that the geometry at the individual level can be devised and modulated to attain dynamic patterns at the population scale.

2. Model

2.1 Theory

We consider a system of N active rigid L-shaped rods (*i.e.* chiral rods). Each rod has width d and two arms; the ratio of the long arm to the short arm, or arm-length ratio, is denoted by α and the angle between them, or arm angle, is denoted by β (Fig. 1). By utilizing energy from the environment, the active rods bear self-sustained motility. In our model, this active motility is modeled by an active force \mathbf{F}_a acting along the long axis of the rods with an amplitude F_a , and an active counterclockwise torque $M_a = F_a l$ acting on the mass center of each rod, where l denotes eccentricity (*i.e.* the effective distance between the center of mass and the midline of the long axis (Fig. 1a)).

Assuming that the motion of the active rods is overdamped, the center-of-mass \mathbf{r}_i and the orientation $\mathbf{u}_i = (\cos \theta_i, \sin \theta_i)$ of rod i satisfy the following equation of motion²¹

$$\begin{aligned} \partial \mathbf{r}_i / \partial t &= \frac{1}{kT} (\mathbf{D}_T \cdot \mathbf{F}_{a,i} + \mathbf{D}_C M_{a,i} - \mathbf{D}_T \cdot \nabla_{\mathbf{r}} U_i), \\ \partial \mathbf{u}_i / \partial t &= \frac{1}{kT} (\mathbf{D}_C \cdot \mathbf{F}_{a,i} + D_R M_{a,i} - D_R \nabla_{\mathbf{u}_i} U_i), \end{aligned} \quad (1)$$

where kT is the effective thermal energy; D_R is the rotational diffusion coefficient; \mathbf{D}_T and \mathbf{D}_C denote respectively the translational and the translation–rotation coupling diffusion tensors, which are defined as $\mathbf{D}_T = D_{\parallel}^{\parallel} \mathbf{u}_i \mathbf{u}_i + D_{\perp}^{\perp} (\mathbf{u}_i \bar{\mathbf{u}}_i + \bar{\mathbf{u}}_i \mathbf{u}_i) + D_{\perp} (\mathbf{I} - \mathbf{u}_i \mathbf{u}_i)$ and $\mathbf{D}_C = D_C^{\parallel} \mathbf{u}_i + D_C^{\perp} \bar{\mathbf{u}}_i$, where \mathbf{I} is the unit tensor and $\bar{\mathbf{u}}_i = (-\sin \theta_i, \cos \theta_i)$. D_{\parallel} , D_{\perp}^{\parallel} , and D_{\perp} denote the translational diffusion coefficients. D_C^{\parallel} and D_C^{\perp} are the translation–rotation coupling coefficients. These diffusion constants are determined by the specific shape of the self-propelled rods.⁴¹ U_i is the potential of rod i resulting from its short-ranged repulsive interaction with

adjacent rods. The interaction of rods is approximated by discretizing each rod into a chain of beads and summing up the pair interactions between the beads.^{39,42,43} The pair interactions between the beads are modeled by the repulsive Yukawa potential.^{44,45} The potential energy of rod i is given by

$$U_i = \sum_{j \neq i} U_{ij} = \frac{U_0}{2} \sum_{j \neq i} \left(\frac{1}{n^2} \sum_{p=1}^n \sum_{q=1}^n \frac{\exp(-r_{pq}^{ij}/\lambda)}{r_{pq}^{ij}} \right), \quad (2)$$

where the amplitude U_0 denotes the potential strength and is set to $200F_a d$ such that the repulsion force is comparable to the active force. λ is the screening length and its value is set to d , r_{pq}^{ij} is the distance between the p -th segment (*i.e.* bead) in rod i and the q -th segment in rod j , and n is the total number of beads in a rod. We focus on the collision-dominated dynamics in dense active chiral suspensions and ignore hydrodynamic interactions and Brownian forces and torques since they are negligible compared to the active forces and torques in the simulation parameter space considered in this study. When driven by a constant active force F_a , an isolated straight rod follows a straight line trajectory as the active torque vanishes while an isolated chiral rod follows a circular path (Fig. 1b), whose radius R is a function of eccentricity l and diffusion coefficients.⁴¹ The period of circular motion is a decreasing function of l , and it is given by

$$T_0 = \frac{4\pi kT}{D_R F_a (2l - d)}. \quad (3)$$

Since l is directly related to the arm-length ratio α and the arm angle β , a rod with larger α or β will have a larger radius R and a larger period T_0 . The limiting case is a straight rod with infinitely large R and T_0 .

2.2 Simulations

We use a numerical method to solve eqn (1). In the simulations, the rod width d , the orientational characteristic time of a single rod $\tau_0 = 1/D_R$ and the thermal energy kT are used as a characteristic length scale, time scale, and energy scale to normalize eqn (1).

We simulate systems having $N = 2500\text{--}6000$ active rods in a square box of size $L_x = L_y = 400d$ with periodic boundary conditions. Typical simulations are run using the Euler method with an integration step $\Delta t = 10^{-4}$ in dimensionless units and last for $\sim 10^6$ integration steps to ensure sufficient statistics are collected during steady phases. In our simulations, the bead diameter d and the length of the short arm ($n_{\text{short}} = 3$) are fixed, and the length of the long arm ($L_{\text{long}} = n_{\text{long}}d$) is varied to control the aspect ratio ($\alpha = n_{\text{long}}/3$) of individual rods. Thus, the area fraction of the L-shaped rod system is represented by $\phi = Nd^2(n_{\text{long}} + n_{\text{short}} - 1)/L_xL_y$. The area fraction of all the simulations is fixed at 20% unless otherwise specified. The initial particle configurations for the simulations are generated by randomly perturbing a configuration of initially perfectly aligned rods for 10^4 time steps. The coordinates, orientations, and velocities of all the rods are recorded every 10 steps.

2.3 Number density

To obtain a smooth local number density field in the system, we use the following grid point method. We place equally spaced virtual grid points in the x and y directions with distance $4d$. Then the number of rods in the vicinity of grid points (cutoff distance $r_c = 50d$) are counted for each grid point. The local number density field ρ at location \mathbf{r} and time t is calculated by

$$\rho(\mathbf{r}, t) = \left\langle \frac{N_d^i}{\pi r_c^2} \right\rangle_i, \quad (4)$$

where N_d^i is the number of neighbors within the threshold distance r_c to the grid point i , and the average is taken over all the grid points whose distance to \mathbf{r} is below $10d$.

2.4 Identification of dynamic phases

We vary the arm-length ratio α and the arm angle β to study the effects of chirality and symmetric geometry on collective dynamics. For varying α , we fix the number of rods and adjust the simulation box size to keep ϕ constant. In each simulation case, we use the Fourier transformation of local density time series at a steady state to estimate the density oscillation period T_d . The local density oscillation period is compared with the individual circulation motion period T_0 in eqn (3). The period deviation $\delta T (= |T_0 - T_d|/T_d)$ is used to distinguish oscillation phases ($\delta T < 10\%$) and non-oscillation phases ($\delta T > 10\%$). The oscillation phases are further classified into strong oscillation (SO) phases ($\delta T < 5\%$) and weak oscillation (WO) phases ($5\% < \delta T < 10\%$).

For non-oscillation states, we follow previous studies^{46–49} to distinguish various phases including laning, turbulent, and jamming by simplified criteria. Specifically, the polar order parameter $P = \left| \sum_{i=1}^N \mathbf{u}_i \cdot \mathbf{n} \right| / N$ is adopted to distinguish between the laning and turbulent phases, with \mathbf{n} being the nematic order indicating the mean orientation of the rods. We choose a threshold value of $P_c = 0.8$ to quantify the boundary between the two phases. Meanwhile, the mean-square displacement

(MSD) $\langle r^2 \rangle$ is used to identify the boundary between the turbulent and jamming phases, where a sharp drop in the mobility represents the jamming onset. We determine the emergence of the jamming phase when the MSD drops over two orders of magnitude from 100 to 1 in units of d^2 .

2.5 Velocity field and vorticity

Given the positions and velocities of all the rods in the model, we can first get the average velocity associated with each grid point by averaging the velocities of the rods whose distances to the grid points are below the threshold $r_c = 50d$. The velocity field $v(x,y)$ at the position (x,y) is then calculated by averaging over all grid points within a cutoff radius of $10d$ from the location (x,y) . Similarly, the vorticity field $\bar{\omega}(x,y)$ is then calculated according to the vorticity associated with the grid point (m_i, n_i) via

$$\begin{aligned} \bar{\omega}(m_i, n_i) = & \frac{v_y(m_i, n_i) - v_y(m_{i-1}, n_i)}{m_i - m_{i-1}} \\ & - \frac{v_x(m_i, n_i) - v_x(m_i, n_{i-1})}{n_i - n_{i-1}}. \end{aligned} \quad (5)$$

Finally, the vorticity strength ψ of the 2D system is defined as the average absolute vorticity over only the areas where individual rods are located, with the empty areas being excluded. It is given by

$$\psi = \frac{1}{N} \sum_i^N \langle |\bar{\omega}| \rangle_i, \quad (6)$$

where $\bar{\omega}$ is the vorticity associated with the grid points, and the brackets denote an average over $\bar{\omega}$ of the neighbor grid points of rod i and steady state simulation time. Of note, the definition of the vorticity strength in eqn (6) is similar to the enstrophy defined previously.²¹

3. Results and discussion

3.1 Spatiotemporal structures of collective oscillation

We first illustrate that chirality in active rod-shaped particles can produce distinct clustering behavior. Consider dense suspensions of chiral L-shaped rods (ESI,† Movie 1) and achiral straight rods (ESI,† Movie 2) with an aspect ratio $\alpha = 2$ and an area fraction of 20%. To visualize and compare the clustering dynamics, we calculate the local density field of rods (see Section 2.3) and plot the time evolution of the local density field as shown in Fig. 2a (ESI,† Movies 3 and 4). Starting from initial homogeneous fluid-like configurations, both achiral straight rods and chiral L-shaped rods can aggregate and form dynamic clusters (shown as local maxima in the local density field plot) after a transient stage (0– $10\tau_0$, Fig. 2a). Consistent with previous studies,^{22,33,50} the achiral straight rods tend to form long-lived, large-scale (> 1000 rods) clusters due to the synergic effects of self-propulsion, excluded volume repulsion, and elongated geometry promoted alignment. In comparison, the chiral L-shaped rods tend to form short-lived ($\sim 2\tau_0$), small-scale (~ 300 rods) clusters.

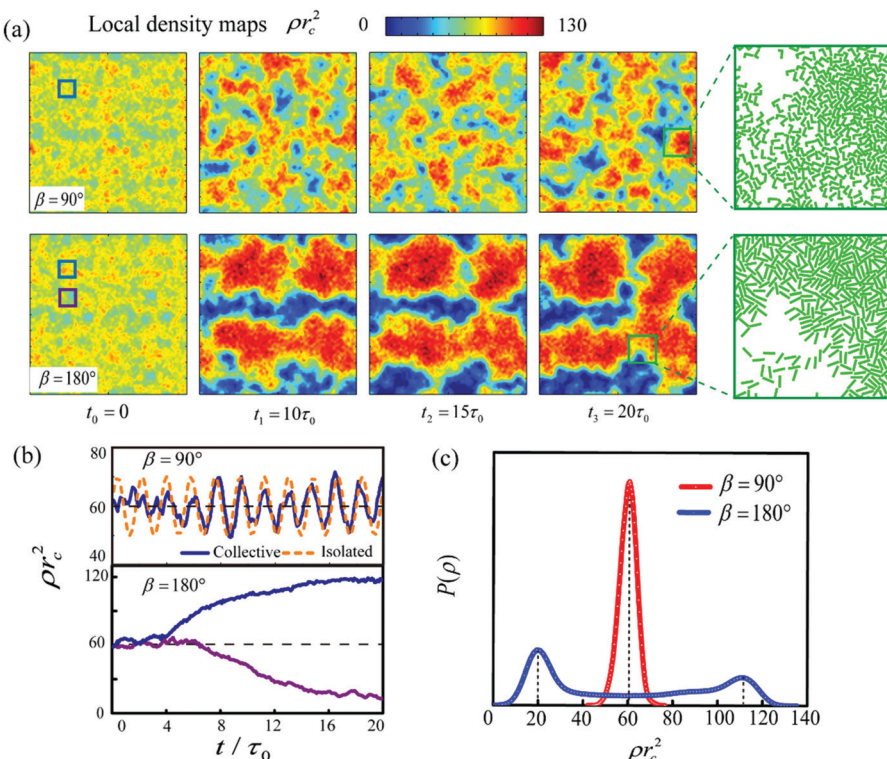


Fig. 2 (a) Time evolution of local density field in the chiral L-shaped rod system (top row) and the achiral straight rod system (bottom row). The elapsed time is provided at the bottom. The rightmost column shows the representative configurations in the steady state in a window of $40d$ length. (b) Local number density at a typical location (the box area in Fig. 2a, $t_0 = 0$) as a function of time in the chiral rod system (top) and the achiral rod system (bottom). Periodic sine-wave like fluctuations of local number density appears in the system of chiral rods in the steady state. A reference curve of a sine wave with period T_0 (eqn (3)) is showed in dashed line in the top figure. Horizontal dashed line represents the global number density. (c) The distributions of local density in the chiral system and the achiral system.

We fix a window in the simulation box and track the time evolution of the local density through the window (Fig. 2b). It can be seen that sine wave-like periodic local density fluctuations emerge in the chiral L-shaped rod system after a transient period ($0-4\tau_0$) before clustering occurs (*i.e.*, the peaks of local density). The local density oscillates around the global mean density given by $\rho = N/L_xL_y$, with peaks and valleys located at around 70 and 50, respectively. Surprisingly, the period of oscillation is approximately equal to that of the circular motion of individual rods (eqn (3)). The local density oscillation phenomena are also found for different combinations of α and β (see ESI,† Fig. S1). In achiral straight rod suspension, the local density in fixed regions steadily increases to plateau ~ 110 in regions where the cluster forms, and decreases towards density plateau ~ 20 where rods are depleted. Since the elongated shape of the straight rods promotes the alignment and dense packing, straight rod systems can form clusters with much denser packing than the L-shaped rods (*i.e.* the plateau value of local density is greater than the peaks of L-shaped rods' local density).

Since local density can often vary strongly at different locations due to dynamic clustering in active systems, we also examine the distribution of local density in both achiral and chiral systems. Consistent with previous studies,^{39,51} the local density distribution of achiral straight rods shows two peaks

located at ~ 20 and ~ 110 , indicating phase separation^{52,53} into a dense phase of well-aligned rods and a fluid phase of translating rods (Fig. 2a rightmost column). The density values where the two peaks located are consistent with the local density plateaus observed in Fig. 2b. On the other hand, the local density distribution of a chiral system only has a single narrow peak at a global average density $\rho \sim 60$, indicating much more uniform local density distribution. The local density in the chiral system is sharply bounded between ~ 50 and ~ 70 , consistent with the observation of fast periodic interconversion between the clustering dense phase and the dilute phase (the peak and valley is shown in Fig. 2b, $\beta = 90^\circ$) in the chiral rod system.

3.2 Collision characteristics and clustering mechanism

To understand distinct clustering behaviors, we compare the collision mechanisms between chiral and achiral rod systems. Achiral straight rods tend to align and aggregate with each other after collision because their straight translational paths and elongated shapes both promote the alignment (Fig. 3a). Therefore, the sizes of the existing straight rod aggregates can easily grow (Fig. 3b top row) after sufficient collision with other aggregates. On the other hand, the chiral L-shape rods perform circular motion, and they tend to depart from each other even when they are close to each other and their long-arms are well

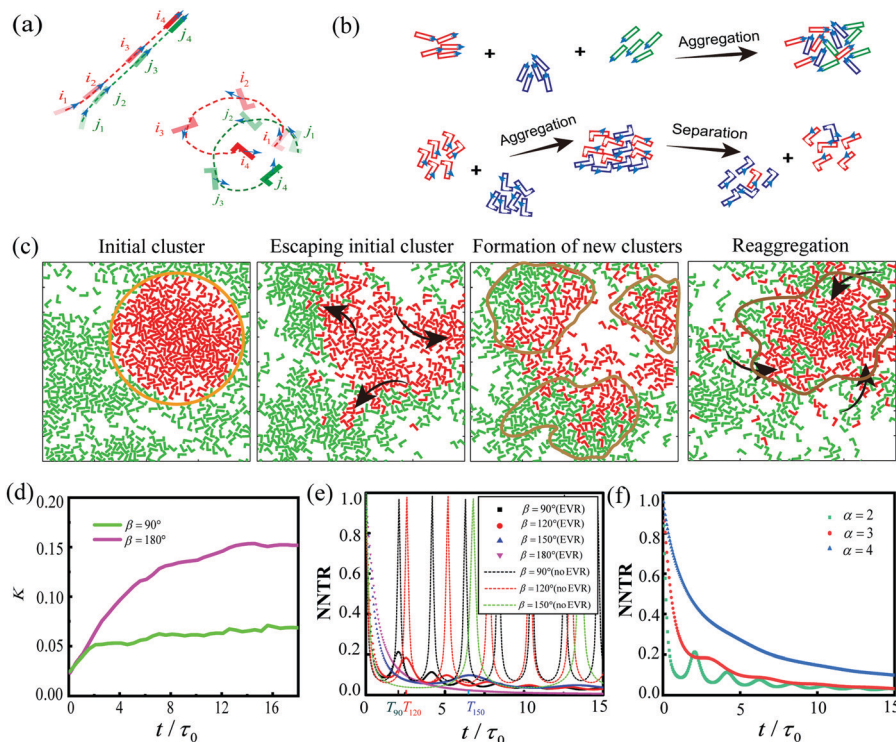


Fig. 3 Motion and collision mechanisms of achiral and chiral rods. (a) Schematics of collision dynamics between two rods. The darkness of the color shade represents the progress of collision, with the lightest hue denotes the initial stage and the darkest the final stage. Dashed lines are their trajectories. The arrow in each rod denotes the direction of active motion. (b) Schematics of collision and dynamic clustering dynamics between multiple groups of small aggregates. (c) Snapshots of L-shaped rod dynamic clustering behavior in the simulation. From left to right: the initial cluster disintegrated as constituent rods (labeled red) circulate away from each other; three new clusters formed nearby the escaping rods collide with other rods; and a majority of original constituent rods reaggregate near the initial cluster location at the end of one period. (d) The local nematic order parameter K as a function of time for straight rod and L-shaped rod systems. (e and f) The nearest neighbor turnover rate $NNTR$ as a function of time for rods with various β ($\alpha = 3$) and α ($\beta = 90^\circ$). T_{90} , T_{120} , and T_{150} are periods of collective oscillation for rods with $\beta = 90^\circ$, 120° , and 150° , respectively.

aligned at the beginning (Fig. 3a bottom row). As a result, after the small aggregates of the L-shaped rods collide together and merge into larger aggregates, larger aggregates are highly unstable and will quickly split into smaller aggregates (Fig. 3b bottom row). Also note that circulation motion enables the chiral rods to re-unite after the separation. The understanding of collision dynamics among several chiral L-shape rods can immediately shed light on the clustering behavior in dense suspension (Fig. 3c). Consider an initial cluster consisting of L-shaped rods (Fig. 3c left). As the constituent L-shaped rods undergo circular motion, mostly the constituent rods quickly escape from the initial cluster, causing the initial cluster to disintegrate (Fig. 3c middle left). In the meantime, the escaping L-rods can collide with other rods in the way and together form a new cluster nearby (Fig. 3c middle right). At the end of one period of circular motion, a majority of original constituent rods circulate back, meet their old neighbors, and re-form a new cluster near the original position of the initial cluster (Fig. 3c right). Owing to individual rod's periodic circular motion, the small aggregates of the L-shaped rods repeat the cycle of collision, merge, split, and reform, thus explaining the periodic oscillation of local density in a fixed region (Fig. 2b). In other words, the circulation induced periodic separation and proximity among the rods is directly responsible for periodic, collective oscillatory motion of chiral rods.

We now draw more comparisons with achiral straight rods to illustrate distinct features of oscillatory collective motion of L-shaped rods. It can be seen that the straight rods tend to form ordered, densely packed, and stable clusters because their elongated geometry promotes the packing and alignment. The chiral L-shaped rods tend to form less ordered and dense clusters because their asymmetric geometry weakens the promotive effect as in straight rods. Furthermore, the circular motion can cause periodic separation and proximity among rods and plays a critical role in determining the dynamic clustering behavior: on the one hand, periodic separation drives the rods to leave newly formed clusters, thus limits the size and life span of the clusters; on the other hand, periodic proximity can bring the rods back together and re-form a new cluster periodically.

To quantitatively characterize the clustering mechanism, we introduce a local nematic order parameter⁵⁴

$$K(t) = \frac{1}{5N} \sum_i^N \sum_{j \in \text{neigh}_i} \cos[2(\theta_j^t - \theta_i^t)], \quad (7)$$

where neigh_i represents the set of the nearest 5 neighbors surrounding the rod i . $K = 0$ and $K = 1$ correspond to the perfectly isotropic and nematic states, respectively. The time-dependent

behavior of K (Fig. 3d) indicates that a clear local nematic order develops in the achiral straight rod systems, whereas the chiral rod systems can hardly develop a nematic order due to their asymmetric geometry and circular motions.

Motivated by the re-union phenomenon of old neighbors in L-shaped rod systems, we examine the nearest neighbor identity dynamics to capture the circulation induced periodic separation and proximity effect among the rods. We define the nearest neighbor turnover rate by

$$\text{NNTR}(t) = \frac{1}{20} \langle \text{NN}_{20}^j(t_0) \theta \text{NN}_{20}^j(t_0 + t) \rangle, \quad (8)$$

where $\text{NN}_{20}^j(t)$ is the identity of the nearest 20 neighbors surrounding the rod j , $A \theta B$ represents the number of the same identities between A and B. NNTR takes a value close to 1 when the majority of 20 nearest neighbors remain the same after time t and takes a smaller value when the identities of nearest neighbor significantly change.

We now examine the neighbor turnover rate dynamics for systems with different α and β at a fixed area fraction. For straight rod systems ($\beta = 180^\circ$, Fig. 3e), NNTR gradually decreases to zero as time elapses, simply because the individual rods are gradually departing their old neighbors. For a chiral rod system, NNTR first quickly decreases to a local minimum valley due to the circular motion induced separation, then it increases to a local peak value after one period of circular motion. This is because the circular motion brings a portion of original neighbors back for re-union as the ‘periodic proximity’ effect. Note that excluded volume repulsion (EVR) between rods alters the periodic circular trajectory when rods collide and will prevent the re-union of exactly all old neighbors (*i.e.* prevent $\text{NNTR}(t)$ from increasing to exactly 1). If we remove the particle interactions as shown in eqn (1), the circular motion can bring exactly all the old neighbors for re-union, with NNTR increasing to 1 at the end of each period (Fig. 3e). As we vary α and β (Fig. 3e and f), we find that the periodic reversal of NNTR is most pronounced (*i.e.* deep valley and steep increasing) for short L-shaped rods (small α) and L-shaped rods with near right angles ($\beta = 90^\circ$). This is because the periodic separation and the proximity effect is more pronounced at smaller α and $\beta = 90^\circ$, which we will explain in the next section. As α increases to 4 or β gets closer to 180° such that the individual bent rods progressively become straight, and NNTR(t) declines steadily without significant periodic reversal.

3.3 Phase diagram

We now establish a phase diagram to illustrate how the arm-length ratio α and arm angle β control the collective dynamics of the active rods (Fig. 4a). When $\beta < 160^\circ$, oscillation phases emerge in systems with most of the α we have considered. To capture the transitional phases between achiral rods and chiral rods, we distinguish the oscillation phases between strong oscillation (SO) and weak oscillation (WO), where the SO phases have period deviation from the individual circular motion period within 5%, and the WO phases have period deviation from the individual circular motion period between 5% and

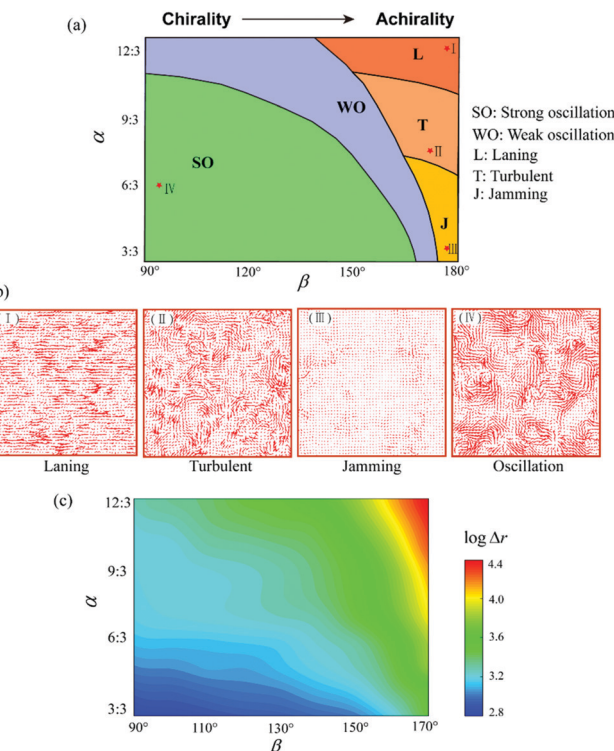


Fig. 4 (a) Phase diagram with varying α and β at fixed area fraction 20%. Phases are classified into (I) laning phase, (II) turbulent phase, (III) jamming phase, and (IV) oscillation phase (strong and weak). The corresponding coarse-grained maps of the velocity fields in various phases (a) are shown in (b). (c) Single-period deviation Δr (eqn (9)) reflecting the strength of the periodic separation and proximity effect in α - β plane.

10% (see Section 2.4). For the L-shaped rod with $\beta = 90^\circ$, the SO phases are observed when the aspect ratio ranges from 1 to 10/3 but the WO phase emerges when α further increases. As β increases further, the SO phases switch to the WO phases, and the transition occurs more easily (occurs at smaller β) for longer L-shaped rods. At fixed β below 170° , increasing α can also weaken the oscillation and lead to the SO-to-WO transition.

At a limit of $\beta = 180^\circ$ (*i.e.*, straight rods), the jamming phase (J), turbulent phase (T), and laning phase (L) can emerge as α increases, consistent with previous studies.^{46–49} These phase boundaries are calculated using simplified criteria from existing studies to demonstrate the qualitative effects of α and β (see Section 2.4 for details).^{46–49} The observations at different α and β suggest that the competition between the periodic separation and proximity effect and the alignment effect plays key roles in the formation of different phases. The periodic separation and proximity effect from circular motion is the strongest at small α and $\beta \sim 90^\circ$ when the circular motion has a small radius and period; the effect decreases as α or β increases. The alignment effects due to the elongated shape are the opposite: it is the strongest at large α and $\beta \sim 180^\circ$; it decreases as α or β decreases. The periodic separation and proximity effect favors the formation of oscillation phases whereas the alignment effect favors the formation of non-oscillation, stable clusters. Therefore, by varying α and β , the comparative strength of the two effects is tuned to produce different dynamic phases.

After determining the different phases with respect to α and β , we now provide a single-particle level explanation for the SO-to-WO transition and the final disappearance of oscillation phases. Since the oscillation phases result from the circular motion induced periodic separation and proximity, we characterize the strength of this effect using the single-period deviation defined by

$$\Delta r = \frac{1}{R} \langle \|r(t_0 + T_0) - r(t_0)\| \rangle_{t_0, N}, \quad (9)$$

where $r(t)$ is the position of rods at time t , T_0 is the single period of rods in the system, R is the radius of circular motion, and $\| \cdot \|$ represents the norm of vector. To rationalize the use of Δr as the proxy measure of the induced periodic separation and proximity effect, we consider the following examples. A single isolated rod performing circular motion will have periodic deviation of 0 since the circular motion brings itself back after one period. For non-isolated rods, interaction with neighboring rods will cause deviation from circular trajectory, thus weakening the induced periodic separation and proximity effect, and lead to larger Δr . As shown in Fig. 4c, there is a close relationship between oscillation phases and Δr . At small α and β where the SO phases are observed, Δr has overall smaller values around 20. In other words, as individual rods have smaller deviation from their circular motion trajectory, the collective groups of rods exhibit oscillatory motion. At intermediate values of α and β where the WO phases emerge, Δr increases to around 38. At larger α and β where the oscillation phases disappear, Δr has overall larger values around 80. There are two contributing effects from α and β on larger Δr and attenuation of oscillation. First, the rods with larger radius of the circulation trajectory will have higher chances to collide with more neighbors and derail from its circular trajectory, and therefore larger Δr . Second, the rods with larger α and β can align with their neighbors more easily, which also cause relatively larger deviation from their original circular trajectories after colliding with neighbors.

3.4 Vortex characteristics

Emergence of vortices from collective motion is commonly observed in a broad class of active systems.^{12,21,46,55–58} Here we show that strong vortices also appear in our chiral system. Fig. 5 shows the mean velocity distribution $v(r)$ and its associated vorticity field (see Section 2.5) given by $\bar{\omega} = [\nabla \times v(r)]$ for the L-shaped ($\beta = 90^\circ, 150^\circ$) and straight rods. In straight rod systems such as bacteria suspensions, swirling vortices can be spontaneously organized in a confined environment and other conditions like the shape and number of rods need to be met.^{59,60} But the chiral systems tend to form vortex structures more easily. Similar to the concept of enstrophy,²¹ we have defined the vorticity strength ψ (see Section 2.5). By characterizing ψ at different α and β , we find that the variations of vorticity strength ψ are almost self-explanatory in terms of the dynamic phases (Fig. 5d): vorticity strength is the largest at small α and β where the SO phases are formed; ψ decreases at larger α and β as the phases transition to WO or non-oscillation phases. From the perspective of particle dynamics, short and right-angle L-shaped rods have short-period,

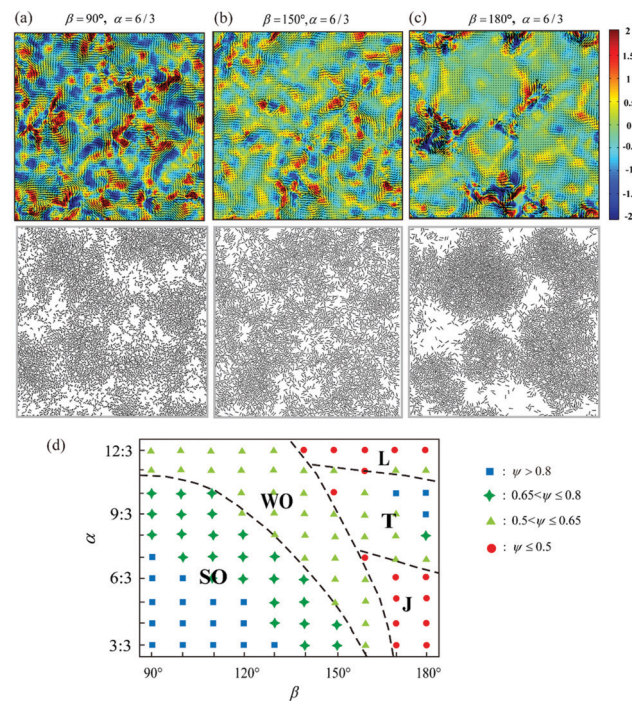


Fig. 5 Instantaneous vorticity (color) and velocity (black arrows) field in the system of L-shaped rods with (a) $\beta = 90^\circ$, (b) $\beta = 150^\circ$, and straight rods (c). The corresponding particle configurations are shown in corresponding bottom panels. (d) Vorticity strength ψ of the system for various α and β . They are represented by different symbols. The phases of the steady-state are also marked in the diagram.

small-radius circular motion that contributes to the formation of strong vortex structures. Larger α and β will enhance the alignment effect that leads to weak oscillation phases and thus a smaller vorticity strength. As Δr (Fig. 4c) and vorticity strength ψ show similar dependence on α and β , it implies that the circular motion of individual rods is the common factor leading to both oscillation and vortex formation. Note that collective straight rods with $\alpha = 9/3$ and $10/3$ also exhibit a strong vortex state due to the formation of the turbulent phase (Fig. 4a and b).^{21,49}

4. Conclusions

We have studied the collective dynamics of a 2D system consisting of self-propelled chiral rods. Compared with achiral straight rods, the dense suspension of chiral L-shaped rods will form small-sized, short-lived, and most strikingly, periodic oscillatory dynamic clusters. The distinct collective motions in achiral straight rods and chiral L-shaped rods can be understood by their distinct collision and aggregation mechanisms. The major factors leading to the formation of oscillation in the L-shaped rods are the periodic separation and proximity induced by circular motions of individuals. We construct non-equilibrium phase diagrams based on the arm-length ratio and arm angle. By characterizing the local nematic order, the nearest neighbor turnover rate, and the single-period deviation, we show that the comparative strength of the periodic separation and proximity effect arising from chirality and the

alignment effect arising from an elongated shape drives the formation of oscillatory phases and non-oscillatory phases. The chiral rod systems also exhibit significant vortex structures compared to the achiral straight rod systems. The strength of vorticity and oscillatory collective motion exhibit similar dependency on the arm-length ratio and arm angle. Our findings help understand the dynamic features in various active chiral systems. The emerging oscillatory phases and vortex structures might find potential applications ranging from invisibility cloaks to nanorobotics.^{61,62}

Finally, it should be pointed out that to further elucidate the mechanisms underpinning the collective motion of living chiral objects, biological complexity involving hydrodynamics, noise and chemotaxis usually needs to be considered. In addition, other asymmetric geometries and individual dynamic characteristics may also give rise to unknown collective phenomena. These issues merit further studies to understand the role of chirality in collective dynamics.

Conflicts of interest

There are no conflicts of interest to declare.

Acknowledgements

Supports from the National Natural Science Foundation of China (Grant No. 11620101001, 11672161, and 11432008) are acknowledged.

References

- R. Dreyfus, J. Baudry, M. L. Roper, M. Fermigier, H. A. Stone and J. Bibette, *Nature*, 2005, **437**, 862–865.
- G. H. Koenderink, Z. Dogic, F. Nakamura, P. M. Bendix, F. C. MacKintosh, J. H. Hartwig, T. P. Stossel and D. A. Weitz, *Proc. Natl. Acad. Sci. U. S. A.*, 2009, **106**, 15192–15197.
- J. Toner and Y. Tu, *Phys. Rev. E: Stat. Phys., Plasmas, Fluids, Relat. Interdiscip. Top.*, 1998, **58**, 4828.
- A. K. Boal, F. Ilhan, J. E. DeRouchey, T. Thurn-Albrecht, T. P. Russell and V. M. Rotello, *Nature*, 2000, **404**, 746–748.
- D. Bi, X. Yang, M. C. Marchetti and M. L. Manning, *Phys. Rev. X*, 2016, **6**, 021011.
- Y. Yang and M. A. Bevan, *ACS Nano*, 2018, **12**, 10712–10724.
- S. Z. Lin, B. Li, G. Lan and X. Q. Feng, *Proc. Natl. Acad. Sci. U. S. A.*, 2017, **114**, 8157–8162.
- M. Czajkowski, D. Bi, M. L. Manning and M. C. Marchetti, *Soft Matter*, 2018, **14**, 5628–5642.
- M. F. Copeland and D. B. Weibel, *Soft Matter*, 2009, **5**, 1174–1187.
- K. Drescher, J. Dunkel, L. H. Cisneros, S. Ganguly and R. E. Goldstein, *Proc. Natl. Acad. Sci. U. S. A.*, 2011, **108**, 10940–10945.
- A. Sokolov and I. S. Aranson, *Phys. Rev. Lett.*, 2009, **103**, 148101.
- G. Kokot and A. Snejhko, *Nat. Commun.*, 2018, **9**, 2344.
- M. Mijalkov and G. Volpe, *Soft Matter*, 2013, **9**, 6376–6381.
- J. Yan, M. Han, J. Zhang, C. Xu, E. Luijten and S. Granick, *Nat. Mater.*, 2016, **15**, 1095–1099.
- A. Kaiser, K. Popowa, H. Wensink and H. Löwen, *Phys. Rev. E: Stat., Nonlinear, Soft Matter Phys.*, 2013, **88**, 022311.
- A. Ciach, J. Pękalski and W. T. Góźdż, *Soft Matter*, 2013, **9**, 6301–6308.
- T. Vicsek and A. Zafeiris, *Phys. Rep.*, 2012, **517**, 71–140.
- S. Z. Lin, S. Ye, G. K. Xu, B. Li and X. Q. Feng, *Biophys. J.*, 2018, **115**, 1826–1835.
- H. Wioland, F. G. Woodhouse, J. Dunkel and R. E. Goldstein, *Nat. Phys.*, 2016, **12**, 341–345.
- V. Narayan, S. Ramaswamy and N. Menon, *Science*, 2007, **317**, 105–108.
- H. H. Wensink, J. Dunkel, S. Heidenreich, K. Drescher, R. E. Goldstein, H. Löwen and J. M. Yeomans, *Proc. Natl. Acad. Sci. U. S. A.*, 2012, **109**, 14308–14313.
- F. Peruani, A. Deutsch and M. Bär, *Phys. Rev. E: Stat., Nonlinear, Soft Matter Phys.*, 2006, **74**, 030904.
- A. Deblais, T. Barois, T. Guerin, P.-H. Delville, R. Vaudaine, J. S. Lintuvuori, J.-F. Boudet, J.-C. Baret and H. Kellay, *Phys. Rev. Lett.*, 2018, **120**, 188002.
- H. H. Wensink and H. Löwen, *Phys. Rev. E: Stat., Nonlinear, Soft Matter Phys.*, 2008, **78**, 031409.
- H. Jiang and S. X. Sun, *Soft Matter*, 2012, **8**, 7446–7451.
- K. D. Young, *Microbiol. Mol. Biol. Rev.*, 2006, **70**, 660–703.
- L. E. Martinez, J. M. Hardcastle, J. Wang, Z. Pincus, J. Tsang, T. R. Hoover, R. Bansil and N. R. Salama, *Mol. Microbiol.*, 2016, **99**, 88–110.
- B. Liu, M. Gulino, M. Morse, J. X. Tang, T. R. Powers and K. S. Breuer, *Proc. Natl. Acad. Sci. U. S. A.*, 2014, **111**, 11252–11256.
- W. R. DiLuzio, L. Turner, M. Mayer, P. Garstecki, D. B. Weibel, H. C. Berg and G. M. Whitesides, *Nature*, 2005, **435**, 1271–1274.
- P. Denissenko, V. Kantsler, D. J. Smith and J. Kirkman-Brown, *Proc. Natl. Acad. Sci. U. S. A.*, 2012, **109**, 8007–8010.
- B. M. Friedrich and F. Jülicher, *Phys. Rev. Lett.*, 2009, **103**, 068102.
- T. W. Su, L. Xue and A. Ozcan, *Proc. Natl. Acad. Sci. U. S. A.*, 2012, **109**, 16018–16022.
- B. Liebchen and D. Levis, *Phys. Rev. Lett.*, 2017, **119**, 058002.
- H. B. Kolli, G. Cinacchi, A. Ferrarini and A. Giacometti, *Faraday Discuss.*, 2016, **186**, 171–186.
- M. Y. Ben Zion, X. He, C. C. Maass, R. Sha, N. C. Seeman and P. M. Chaikin, *Science*, 2017, **358**, 633–636.
- X. Li, B. Caswell and G. E. Karniadakis, *Biophys. J.*, 2012, **103**, 1130–1140.
- Y. Yang, J. Liang, F. Pan, Z. Wang, J. Zhang, K. Amin, J. Fang, W. Zou, Y. Chen, X. Shi and Z. Wei, *Nat. Commun.*, 2018, **9**, 3808.
- H. H. Wensink and C. Ferreiro-Córdova, *Soft Matter*, 2017, **13**, 3885–3893.
- M. Abkenar, K. Marx, T. Auth and G. Gompper, *Phys. Rev. E: Stat., Nonlinear, Soft Matter Phys.*, 2013, **88**, 062314.
- F. Ginelli, F. Peruani, M. Bär and H. Chaté, *Phys. Rev. Lett.*, 2010, **104**, 184502.
- F. Kümmel, B. ten Hagen, R. Wittkowski, I. Buttinoni, R. Eichhorn, G. Volpe, H. Löwen and C. Bechinger, *Phys. Rev. Lett.*, 2013, **110**, 198302.
- Y. Yang and M. A. Bevan, *J. Chem. Phys.*, 2017, **147**, 054902.

- 43 Y. Yang, V. Marceau and G. Gompper, *Phys. Rev. E: Stat., Nonlinear, Soft Matter Phys.*, 2010, **82**, 031904.
- 44 A. Kaiser, A. Peshkov, A. Sokolov, B. ten Hagen, H. Löwen and I. S. Aranson, *Phys. Rev. Lett.*, 2014, **112**, 158101.
- 45 J. Bialké, T. Speck and H. Löwen, *Phys. Rev. Lett.*, 2012, **108**, 168301.
- 46 C. Dombrowski, L. Cisneros, S. Chatkaew, R. E. Goldstein and J. O. Kessler, *Phys. Rev. Lett.*, 2004, **93**, 098103.
- 47 S. Henkes, Y. Fily and M. C. Marchetti, *Phys. Rev. E: Stat., Nonlinear, Soft Matter Phys.*, 2011, **84**, 040301.
- 48 A. Martín-Gómez, D. Levis, A. Díaz-Guilera and I. Pagonabarraga, *Soft Matter*, 2018, **14**, 2610–2618.
- 49 H. H. Wensink and H. Löwen, *J. Phys.: Condens. Matter*, 2012, **24**, 464130.
- 50 F. Ginot, I. Theurkauff, F. Detcheverry, C. Ybert and C. Cottin-Bizonne, *Nat. Commun.*, 2018, **9**, 696.
- 51 I. R. Bruss and S. C. Glotzer, *Phys. Rev. E*, 2018, **97**, 042609.
- 52 G. S. Redner, M. F. Hagan and A. Baskaran, *Phys. Rev. Lett.*, 2013, **110**, 055701.
- 53 J. Stenhammar, D. Marenduzzo, R. J. Allen and M. E. Cates, *Soft Matter*, 2014, **10**, 1489–1499.
- 54 P. Kraikivski, R. Lipowsky and J. Kierfeld, *Phys. Rev. Lett.*, 2006, **96**, 258103.
- 55 L. Giomi, *Phys. Rev. X*, 2015, **5**, 031003.
- 56 K. Kruse, J. F. Joanny, F. Jülicher, J. Prost and K. Sekimoto, *Phys. Rev. Lett.*, 2004, **92**, 078101.
- 57 H. Jiang, H. Ding, M. Pu and Z. Hou, *Soft Matter*, 2017, **13**, 836–841.
- 58 A. Bricard, J.-B. Caussin, D. Das, C. Savoie, V. Chikkadi, K. Shitara, O. Chepizhko, F. Peruani, D. Saintillan and D. Bartolo, *Nat. Commun.*, 2015, **6**, 7470.
- 59 E. Lushi, H. Wioland and R. E. Goldstein, *Proc. Natl. Acad. Sci. U. S. A.*, 2014, **111**, 9733–9738.
- 60 D. Nishiguchi, I. S. Aranson, A. Snezhko and A. Sokolov, *Nat. Commun.*, 2018, **9**, 4486.
- 61 P. Alitalo and S. Tretyakov, *Mater. Today*, 2009, **12**, 22–29.
- 62 L. Zeng and R. Song, *Sci. Rep.*, 2017, **7**, 3253.